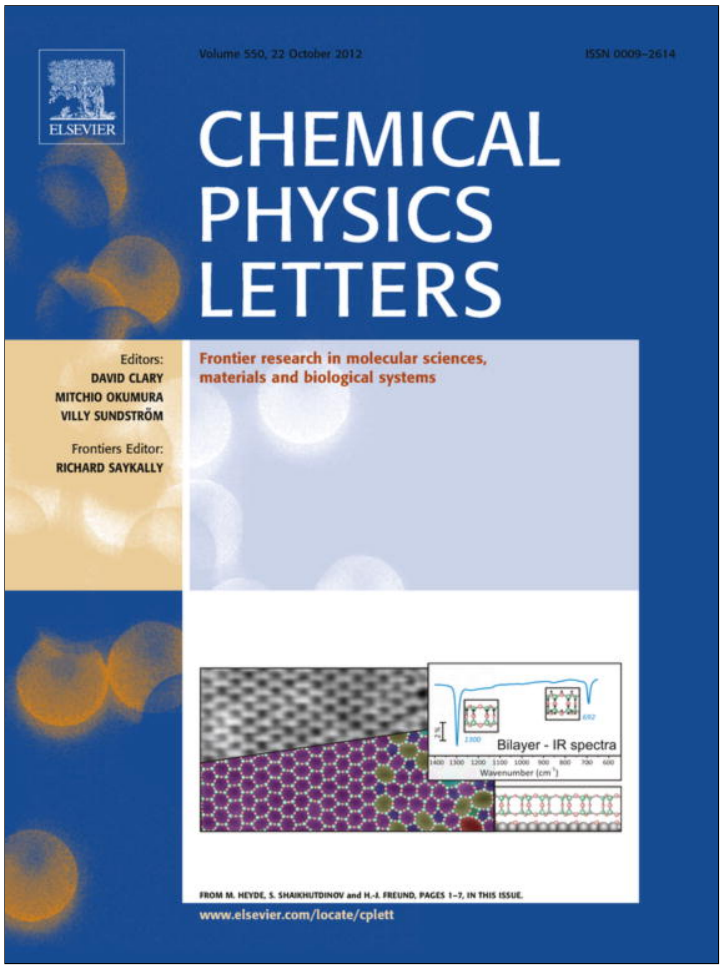

Chemical Physics Letters 550 (2012) 79–82

Contents lists available at SciVerse ScienceDirect

Chemical Physics Letters

journal homepage: www.elsevier.com/locate/cplett

UV/Vis spectroscopy of C_{60} embedded in water ice

Steven H. Cuylle [a], Harold Linnartz [a,*], John D. Thrower [b]

[a] Sackler Laboratory for Astrophysics, Leiden Observatory, University of Leiden, P.O. Box 9513, NL 2300 RA Leiden, The Netherlands
[b] Department of Physics & Astronomy, Aarhus University, 8000 Aarhus C, Denmark

ARTICLE INFO

Article history:
Received 4 July 2012
In final form 31 August 2012
Available online 8 September 2012

ABSTRACT

Electronic solid state spectra are recorded for C_{60} embedded in 40 K water ice using broad band direct absorption spectroscopy, and assigned with reference to existing matrix data. The results are interesting in view of the recent gas phase detection of fullerenes in the interstellar medium and provide a realistic solid state signature to search for frozen C_{60} in space.

1. Introduction

Decades of dedicated fullerene research have resulted in a wealth of spectroscopic and dynamical information on fullerenes and carbon nanotubes [1,2]. Their special properties have been intensely investigated and various applications have been proposed ranging from e.g., solar cell applications [3] to targeted drug delivery [4]. With their detection on Earth, fullerenes were also proposed to be present in the interstellar medium. First observations that hinted in this direction were reported in Refs. [5,6]. An unambiguous identification was reported by Cami et al. who observed both C_{60} and C_{70} in the unusual planetary nebula Tc1 by comparing Spitzer-IRS and laboratory infrared emission gas phase spectra of vibrational modes [7]. Since this discovery C_{60} has been detected along other lines of sight, including reflection nebulae [8], embedded young stellar objects, a Herbig Ae/Be star, a post-asymptotic giant branch star [9] and H-deficient RCB stars [10], indicating that fullerenes may be widespread in space. This is actually not that surprising given the fact that many carbon bearing species have been identified in the interstellar medium and fullerenes belong to the most stable carbon species (see also [11] and references therein); they are predicted to carry up to 1.5% of the available carbon in inter and circumstellar environments. Even more recently, Evans et al. [12] reported the possible detection of solid-phase C_{60} in the binary XX Oph. Indeed, at the low temperatures of dark interstellar clouds, C_{60} molecules are expected to stick together and to form agglomerates, as has been observed for polycyclic aromatic hydrocarbons (PAHs) [13]. It also has been proposed that PAHs, as large non-volatile species, will accrete in dense interstellar clouds onto cold dust grains together with other species – most noticeably water – to become embedded in interstellar ices. This idea has been extensively discussed in Refs. [14–16] and is consistent with the astronomical observation that strong infrared emission lines originating from UV excited PAHs are not visible from such clouds, as in the ice matrix the responsible vibrational modes are quenched. Here, volatile molecules freeze out, forming layers of ice on micrometer sized dust grains [17], providing a molecule reservoir. Upon external chemical triggers, i.e., UV photon irradiation, ice species participate in a solid state chemical reaction network (see e.g., Refs. [18,19]). A similar evolution is expected for C_{60} and for this reason the UV/Vis spectrum of C_{60} embedded in water ice has been studied. This spectrum provides, in essence, the spectroscopic tool with which to search for C_{60} embedded in water ice.

2. Experiment

The experiments are performed with OASIS, our Optical Absorption Setup for Ice Spectroscopy that has been described in detail in Ref. [15]. The setup consists of a high vacuum chamber (3×10^{-7} -mbar) in which ices are grown on a thermally controlled MgF_2 deposition window. The window is mounted on top of the cold head of a closed-cycle helium cryostat. An integrated tip heater allows accurate temperature control between 13 and 325 K. Here, experiments are performed at an astronomically relevant and fixed temperature of 40 K. The co-deposition system for H_2O (Milli-Q, purified by three freeze–pump-thaw cycles) and C_{60} (Sigma–Aldrich, 99%) consists of an external manifold with a dosing valve for the water matrix and a resistively heated oven affixed to the end of the line for C_{60}. Heating the oven with 2–3 W is sufficient for thermal evaporation of the C_{60} without chemically altering it. This allows a homogeneous mixing of both constituents, typically in a C_{60}:H_2O ratio of roughly 1:5000. During deposition, the ice thickness is monitored using a HeNe laser based interferometric system. Typical deposition rates amount to about 3 nm/s and final ice thicknesses are between 0.5 and 1 μm. The ice is spectroscopically investigated by focusing white light of a Xe-arc lamp through the ice onto the inlet of an Andor Shamrock 303i spectrometer. This monochromator disperses the light in a range from 200–1000 nm with a best spectral resolution of 0.55 nm. Given

* Corresponding author.
E-mail address: Linnartz@strw.leidenuniv.nl (H. Linnartz).

0009-2614/$ - see front matter © 2012 Elsevier B.V. All rights reserved.
http://dx.doi.org/10.1016/j.cplett.2012.08.072

Table 1
Spectral parameters of C_{60} embedded in water ice (C_{60}:$H_2O \sim 1$:5000) at 40 K.

Stronger and broad features (~200–400 nm)							
Label	ν_{H_2O} $(cm^{-1})_{vac}$	λ_{H_2O} $(nm)_{vac}$	FWHM (cm^{-1})	$\nu_{Ne/hex\ matrix}$ $(cm^{-1})_{vac}$[a,b]	ν_{gas} $(cm^{-1})_{vac}$	Transition	$\Delta\nu_{H_2O-matrix}$ (cm^{-1})
A	45952(130)	217.6	2189	$47633(228)_{hex}$	–	$8^1T_{1u}-{}^1A_g\ 0_0^0$	−1681
B	42256(111)	236.7	3617	$43988(194)_{hex}$	–	$7^1T_{1u}-{}^1A_g0_0^0$	−1732
C	38753(94)	258.0	2961	$38983(153)_{hex}$	–	$6^1T_{1u}-{}^1A_g0_0^0$	−230
D	34270(75)	291.8	4756	$34257(12)_{Ne}$ $33013(11)_{Ne}$	–	$5^1T_{1u}-{}^1A_g0_0^04^1T_{1u}-{}^1A_g0_0^0$	−622
E	30618(61)	326.6	1382	$30969(10)_{Ne}$	–	$3^1T_{1u}-{}^1A_g0_0^0$	−351
F	29737(57)	336.3	2619			Unknown	–
G	27116(48)	368.8	2901	$26604(7)_{Ne}$	–	$2^1T_{1u}-{}^1A_g0_0^0$(tentative)	512
Weaker and narrow features(~365–420 nm)							
Label	ν_{H_2O} $(cm^{-1})_{vac}$	λ_{H_2O} $(nm)_{vac}$	FWHM (cm^{-1})	$\nu_{Ne-/hex\ matrix}$ $(cm^{-1})_{vac}$[b,c]	ν_{gas} $(cm^{-1})_{vac}$[d,e]	Transition	$\Delta\nu_{H_2O-matrix/gas}$ (cm^{-1})
a	28088(52)	356.0	159	$28097(8)_{Ne}$	–	$2^1G_u-{}^1A_g + h_g(7)$ (tentative)	−9/–
b	27828(51)	359.4	323	$27941(8)_{Ne}$	–	$2^1G_u-{}^1A_g + h_g(6)$ (tentative)	−113/–
c	27611(50)	362.2	147	$27747(8)_{Ne}$	–	$2^1G_u-{}^1A_g + h_g(5)$	−136/–
d	27439(50)	364.4	249	$27456(8)_{Ne}$	–	$2^1G_u-{}^1A_g + h_g(4)$	−17/–
e	27156(49)	368.2	357	$27390(8)_{Ne}$	–	$2^1T_{1u}-{}^1A_g + h_g(3)$	−234/–
f	26563(47)	376.5	223	$26853(7)_{Ne}$	–	$2^1T_{1u}-{}^1A_g + h_g(1)$	−290/–
				$26710(7)_{Ne}$		$2^1G_u-{}^1A_g0_0^0$	−147/–
g	26367(46)	379.3	164	$26604(7)_{Ne}$	–	$2^1T_{1u}-{}^1A_g0_0^0$	−237/–
h	26160(45)	382.3	150	$26324(7)_{Ne}$	–	$1^1T_{1u}-{}^1A_g + h_g(7)$	−164/–
				$26358(7)_{Ne}$		$1^1T_{1u}-{}^1A_g + a_g(2)$	−198/–
				$26393(7)_{Ne}$		$1^1T_{1u}-{}^1A_g + h_g(8)$	−233/–
i	25942(45)	385.5	219	$26172(7)_{Ne}$	–	$1^1G_{1u}-{}^1A_g + a_g(2)$	−230/–
				$26102(7)_{Ne}$		$1^1T_{1u}-{}^1A_g + h_g(6)$	−160/–
j	25680(44)	389.4	224	$25935(7)_{Ne}$	25934	$1^1T_{1u}-{}^1A_g + h_g(5)$	−255/−254
k	25311(43)	395.1	224	$25550(7)_{Ne}$	25544	$1^1T_{1u}-{}^1A_g + h_g(3)$	−239/−233
l	25096(42)	398.5	181	$25343(6)_{Ne}$	–	$1^1T_{1u}-{}^1A_g + a_g(1)$	−247/–
m	24892(41)	401.7	158	$25120(6)_{Ne}$	25133	$1^1T_{1u}-{}^1A_g + h_g(1)$	−228/−241
n	24646(41)	405.7	173	$24852(6)_{Ne}$	24858	$1^1T_{1u}-{}^1A_g0_0^0$	−206/−212
o	24469(40)	408.7	154	$24711(6)_{Ne}$	–	$1^1G_u-{}^1A_g0_0^0$	−242/–
p	24248(39)	412.4	215	$24103(58)_{hex}$	–	$2^1G_u-{}^1A_g0_0^0$	145/–
q	23857(38)	419.2	46	$23676(56)_{hex}$	–	$2^1H_u-{}^1A_g + h_g(8)$	181/–

[a] Ne = Ref. [22].
[b] hex = Ref. [21].
[c] Ne = Ref. [23].
[d] gas = Ref. [27].
[e] gas = Ref. [28].

the large spectral range covered here, this yields different absolute accuracies in terms of absolute numbers (cm^{-1}, see Table 1). UV/Vis spectra are recorded every 10 s and several spectra can be added to increase S/N-ratios. A particular benefit of this technique is that a large spectral range can be covered in one run and this allows simultaneous investigation of many spectral features, also in the time domain ensuring a constant ratio between C_{60} and water over the depth in the ice.

3. Results

Figure 1 shows the broadband (200–420 nm) UV/Vis spectrum of C_{60} embedded in water ice. This spectrum has been recorded in a single pass experiment during 10 s. Besides several broad bands in the 200–400 nm region, a rather large number of narrower bands are observed for wavelengths longer than 365 nm. An expanded view of this region is shown in Figure 2. The spectral features show similarities with previously recorded spectra for C_{60} in matrix environments other than water – hexane, *n*-hexane at 77 K, and 3-methylpentane [20,21], Ne and other rare gas matrices at 4 K [22,23] and hexane/polystyrene [24] – and have been assigned in these studies to vibronic transitions. Electronic gas phase spectra of C_{60} have been predicted or measured [25–28], but their accuracy is limited; the predictions are derived from the solid state work (and are not further considered here) and the gas phase measurements concern high temperature environments. For this reason mainly Ne matrix data [22,23] complemented with n-hexane data [21] are used to guide the identification of the bands observed here in a water ice matrix. Ne environments provide the lowest matrix-induced band shifts and this is confirmed in Table 1 for the limited set of bands for which gas phase data are available [22,23,27]; the matrix shifts typically amount to a few tens of cm^{-1} with respect to unperturbed gas phase data. This is comparable with values that have been found for different PAHs [15].

A sequential fit procedure has been applied. The five broader bands (A–E) not overlapping with the weaker features are fit using the χ^2 fitting tool of Origin 8. Here a well educated guess is made for the three initial GAUSSIAN parameters – centre wavelength, integrated absorption area and FWHM – after which the fitting is performed, restricting the centre wavelength to a certain range centered on the peak position obtained found in the different matrix studies. The resulting optimal values are listed in Table 1. As the bands are very broad the accuracy here is limited. This is also reflected in the large variation of derived $\Delta\nu_{H_2O-matrix/gas}$ values for the stronger and broad features. The red wing of the sixth band (F) at 29737 cm^{-1} and the seventh band around 27116 cm^{-1} (G) overlap with the weaker features and a χ^2 method does not work, as a baseline in the 28500–23500 cm^{-1} region is needed to separately fit the partially overlapping narrower bands. Therefore the

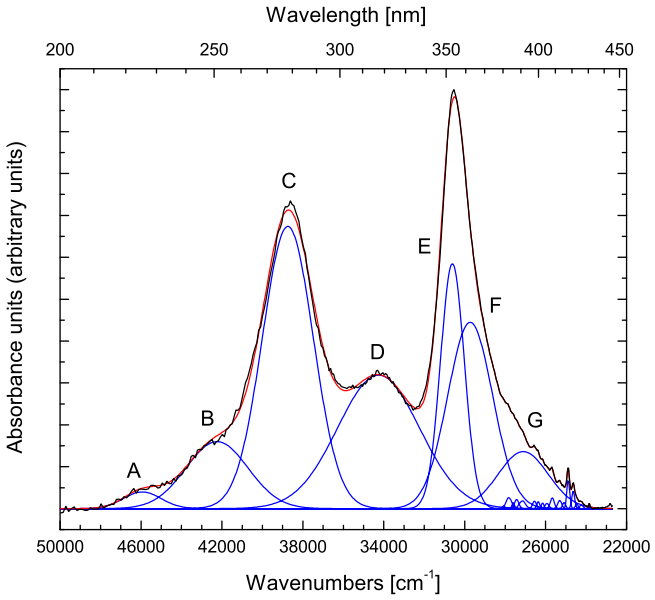

Figure 1. Broadband spectrum of C_{60} embedded in water ice showing Gaussian fits of individual vibronic bands, previously assigned in other matrix environments. The band assignments are reported in the first half of Table 1. The recorded spectrum is shown in black and the result of the overall fit is shown in red. (For interpretation of the references to color in this figure legend, the reader is referred to the web version of this Letter.)

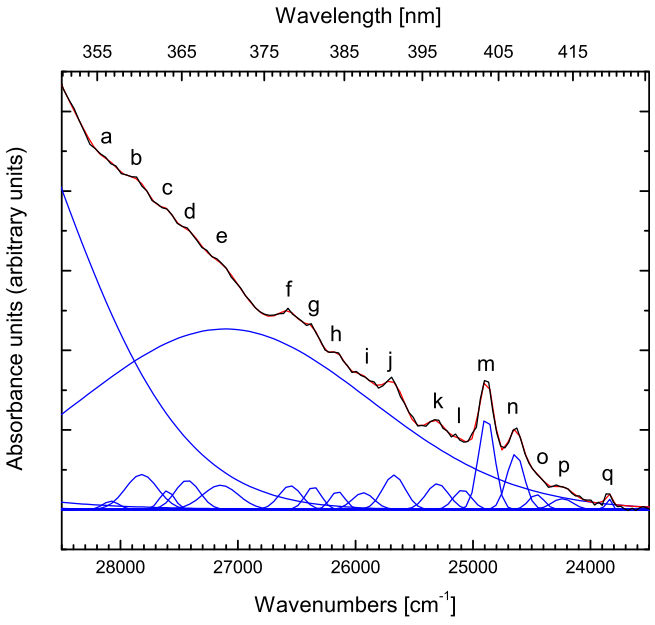

Figure 2. Extended view of Figure 1 showing details of a series of narrower bands including Gaussian fits that follow the assignment of vibronic bands, previously assigned in other matrix environments. The band assignments are reported in the second half of Table 1. The recorded spectrum is shown in black and the result of the overall fit is shown in red. (For interpretation of the references to color in this figure legend, the reader is referred to the web version of this Letter.)

fitting procedure has been adapted in such a way that the G band coincides with the measured spectrum for a number of hand-chosen overlap points, while taking into account the solution for the adjacent Gaussian around 29737 cm^{-1} for the F band. As also the F and G bands overlap, the fit is optimized for one Gaussian per optimization run, and repeated until the fitting parameters remain stable. The G assignment is tentative and possibly incorrect, given the $\Delta\nu$ value that clearly deviates from the other values found for the stronger and broad features.

The subsequent fitting of the narrower features in the 365–425 nm region follows a rather similar method. Most peak positions can be estimated from the spectrum and eventually compared to the data summarized in Ref. [23]. Separate peak-to-peak pair optimization results in 17 Gaussian bands (a–q) fitted to the narrower features. This is shown in Figure 2. The resulting band parameters are listed in Table 1.

4. Assignments

The assignment of the resolved bands is based both on previous matrix and gas phase experiments. As stated before, the latter are essentially unperturbed, but not necessarily more precise because of the high temperature environments in which they have been recorded. The assignments within the different studies reported in literature are largely consistent but not fully in agreement with each other. In order to circumvent further confusion, the present Letter follows the assignments in Ref. [21] and Refs. [22,23]. The strong features labeled A through G – except F represent a series of vibronic transitions into the $^1T_{1u}$ excited state, starting from the ^1A_g ground state of C_{60}. The central band (D) is located at 34270 cm^{-1}, and is composed of the 4^1T_{1u}–$^1A_g0_0^0$ and 5^1T_{1u}–$^1A_g0_0^0$ bands. As found in Ref. [21] it is not possible to resolve both bands and an averaged value is used to calculate the matrix shift. The band at 38753 cm^{-1} (C) corresponds to the 6^1T_{1u}–$^1A_g0_0^0$ transition. The next two transitions involving the 7^1T_{1u} and 8^1T_{1u} levels, around 42256 and 45952 cm^{-1}, respectively, are harder to discern, as towards shorter wavelengths there is an increasing degree of extinction, likely because of UV scattering in the ice, causing spectral features to become significantly weaker. A similar behavior was attributed in Ref. [29] to C_{60} nanoparticles, consistent with a picture in which C_{60} tends to form agglomerates [30]. On the red side, the 3^1T_{1u}–$^1A_g0_0^0$ transition (band E) around 30618 cm^{-1} shows an extensive wing up to 24000 cm^{-1} and needs two additional Gaussians (bands F and G) for appropriate fitting. The only stronger feature reported in this region is the 2^1T_{1u}–$^1A_g0_0^0$ transition and band G is found to be the nearest [31]. The origin of feature F is unknown, but has to be taken into account as without it, no accurate fit can be obtained. Typical shifts with respect to values obtained in a Ne matrix or hexane environment (also listed in Table 1) are of the order of a several hundreds of cm^{-1} and should be regarded with care, given the large uncertainties.

The weaker features labeled a–q, visible in Figure 2, in the 350–420 nm region have been assigned in previous matrix work [21–23] to electronic transitions in the ^1H_u, ^1G_u and $^1T_{1u}$ states with excited Jahn–Teller (h_g) or symmetric (a_g) modes. A comparison of the C_{60}:H_2O spectra to those recorded in a 4 K Ne matrix shows a significant additional broadening as matrix effects in the water ice are indeed expected to be stronger than in a Ne environment. This washes out some of the weakest features that can still be observed in e.g., Ref. [22]. Therefore, special care is needed to extrapolate the Ne matrix results to solid water, particularly as spectral separations are of the order of typical matrix shifts. There are, however, a few distinct spectral features in Figure 2 that facilitate the identification of the subsequent bands and the most probable assignment is presented here. Features m and n around 24892 and 24646 cm^{-1} are stronger than the other bands and likely correspond to the 1^1T_{1u}–$^1A_g + h_g(1)$ and 1^1T_{1u}–$^1A_g0_0^0$ bands as assigned in Ref. [23]. The latter band actually belongs to the series of stronger features discussed before and it should be noted that the FWHM-value is smaller than found for the bands A-G. Furthermore, there is an 'empty' region around 26800 cm^{-1}, between features e and f that is also found in the other matrix studies.

Using this as a starting point, feature o is assigned as 1^1G_u–$^1A_g0_0^0$ through its relative distance from feature n. Features p and q are out of the range discussed in Ref. [23]. Band p can be labeled as 2^1G_u–$^1A_g0_0^0$ following Ref. [21] or 1^1G_u–$^1A_g0_0^0$, according to [22,23]. The latter assignment, however, is in contradiction with the previous o-feature labeling. Based on its distance from feature n, band q is assigned as 2^1H_u–^1A_g + hg(8). Features j and k are due to the 1^1T_{1u}–^1A_g + $h_g(5)$ and 1^1T_{1u}–^1A_g + $h_g(3)$ transitions, respectively, based on their relative strength and distance from feature m [23]. Due to overlap of these two bands, a previously observed feature assigned to 1^1G_u–^1A_g + $h_g(5)$ is not observed here. Feature l is associated with 1^1T_{1u}–^1A_g + $a_g(1)$ and is in between k and m.

Moving to the shorter wavelengths, the assignment of the bands a–i is not trivial, as these features suffer from serious spectral overlaps and multiple transitions effectively result in a single bump in the water ice environment. Feature i may be due to either 1^1G_{1u}–^1A_g + $a_g(2)$ or 1^1T_{1u}–^1A_g + $h_g(6)$ that are difficult to distinguish in the Ne matrix. Feature h is the next peak, and can be associated with three overlapping modes: 1^1T_{1u}–^1A_g + $h_g(7)$, 1^1T_{1u}–^1A_g + $a_g(2)$ and 1^1T_{1u}–^1A_g + $h_g(8)$. Feature g can be linked to the adjacent peak, which is 2^1T_{1u}–$^1A_g0_0^0$. The last peak before the earlier mentioned empty region, peak f, may be due to multiple transitions that form a single peak, comprising the 2^1T_{1u}–^1A_g + $h_g(1)$ and the 2^1G_u–$^1A_g0_0^0$ band in its long wavelength flank. Crossing the empty zone, the measurements of Ref. [23] show three peaks in a strongly sloping baseline. These are linked to features c, d and e in water ice, labeled as 2^1G_u–^1A_g + $h_g(5)$, 2^1G_u–^1A_g + $h_g(4)$ and 2^1T_{1u}–^1A_g + $h_g(3)$, respectively. Finally, features a and b are out of the range of the measurements of Ref. [22], and tentative assignments are 2^1G_u–^1A_g + $h_g(7)$ and 2^1G_u–^1A_g + $h_g(6)$, respectively. Also here it is found that in the water ice environment the bands experience a redshift with respect to the Ne matrix values. A comparison with the available gas phase yields a similar result. This shift is obviously due to the stronger interaction of C_{60} with water compared to Ne, but as this interaction affects both ground and excited state, it is hard to quantify this effect.

5. Astrophysical considerations

The spectrum shown in Figure 1 and the band positions listed in Table 1 provide – in principle - a tool to search for C_{60} embedded in water ice. The spectra presented here are recorded for 40 K, an astronomically relevant temperature, and provide a starting point with which to search for C_{60}:H_2O ice. It is likely that the fullerenes are not formed within the ice, but adsorb onto the grains during the accretion process [32]. A solid state astronomical search for C_{60}:H_2O, using the rather characteristic pattern of the two strong bands C and E around 38 753 and 30 618 cm^{-1}, will be far from trivial, even in the case that C_{60} abundances are sufficiently high. The number of embedded objects with ice surroundings that can be observed in absorption is very limited and it should be noted that wavelengths below 300 nm are not accessible in ground based observations. Also, spectral overlap with electronic transitions of other species, e.g. PAHs, may exist. However, as has been proven in the past, e.g., for anions [33], the most effective strategy to search for new interstellar species and the best way to figure out whether detection is technically feasible is by giving it a try. The present data provide the tools to do so.

Acknowledgement

This Letter has been realized within LASSIE, an interdisciplinary training network within the European Community's 7th Framework Programme under Grant agreement No. 238258.

References

[1] H.W. Kroto, J.R. Heath, S.C. Obrien, R.F. Curl, R.E. Smalley, Nature 318 (1985) 6042.
[2] H.W. Kroto, A.W. Allaf, S.P. Balm, Chem. Rev. 91 (1991) 1213.
[3] N.S. Sariciftci, D. Braun, C. Zhang, V.I. Srdanov, A.J. Heeger, G. Stucky, F. Wudl, Appl. Phys. Lett. 62 (1993) 585.
[4] F. Simon, H. Peterlik, R. Pfeiffer, J. Bernardi, H. Kuzmany, Chem. Phys. Lett. 445 (2007) 288.
[5] M.W. Werner et al., Astrophys. J. Suppl. Ser. 154 (2004) 309.
[6] K. Sellgren, K.I. Uchida, M.W. Werner, Astrophys. J. 659 (2007) 1338.
[7] J. Cami, J. Bernard-Salas, E. Peeters, S.E. Malek, Science 329 (2010) 1180.
[8] K. Sellgren, M.W. Werner, J.G. Ingalls, J.D.T. Smith, T.M. Carleton, C. Joblin, Astrophys. J. 722 (2010) L54.
[9] K.R.G. Roberts, K.T. Smith, P.J. Sarre, Mon. Not. R. Astron. Soc. 421 (2012) 3277.
[10] D.A. Garcia-Hernandez, N.K. Rao, D.L. Lambert, Astrophys. J. 729 (2011) A126.
[11] P. Ehrenfreund, B.H. Foing, Science 329 (2010) 1159.
[12] A. Evans et al., Mon. Not. R. Astron. Soc. 421 (2012) L92.
[13] V.C. Geers, E.F. van Dishoeck, K.M. Pontoppidan, F. Lahuis, A. Crapsi, C.P. Dullemond, G.A. Blake, Astron. Astrophys. 495 (2009) 837.
[14] M.S. Gudipati, L.J. Allamandola, Astrophys. J. 596 (2003) L195.
[15] J. Bouwman, D.M. Paardekooper, H.M. Cuppen, H. Linnartz, L.J. Allamandola, Astrophys. J. 700 (2009) 56.
[16] S.H. Cuylle, E.D. Tenenbaum, J. Bouwman, H. Linnartz, L.J. Allamandola, Mon. Not. R. Astron. Soc. 423 (2012) 1825.
[17] K.I. Öberg et al., Astrophys. J. 740 (2011) 109.
[18] V. Wakelam et al., Space Sci. Rev. 156 (2010) 13.
[19] M.S. Gudipati, L.J. Allamandola, Astrophys. J. 638 (2006) 286.
[20] J.P. Hare, H.W. Kroto, R. Taylor, Chem. Phys. Lett. 177 (1991) 394.
[21] S. Leach et al., Chem. Phys. 160 (1992) 451.
[22] A. Sassara, G. Zerza, M. Chergui, S. Leach, Astrophys. J. Suppl. Ser. 135 (2001) 263.
[23] A. Sassara, G. Zerza, M. Chergui, Phys. Chem. Comm. 28 (2002) 1.
[24] V.S. Pavlovich, E.M. Shpilevsky, J. Appl. Spectrosc. 77 (2010) 335.
[25] J. Catalán, P. Pérez, Nanotubes & Carbon Nanostruct. 10 (2000) 171.
[26] S. Dai, L.M. Toth, G.D. Delcul, D.H. Metcalf, J. Chem. Phys. 101 (1994) 4470.
[27] J. Catalán, Chem. Phys. Lett. 223 (1994) 159.
[28] R.E. Haufler, Y. Chai, L.P.F. Chibante, M.R. Fraelich, R.B. Weisman, R.F. Curl, R.E. Smalley, J. Chem. Phys. 95 (1991) 2197.
[29] V. Apostolopoulou, J. Vakros, C. Kordulis, A. Lycourghiotis, Colloid. Surf. A 349 (2009) 189.
[30] I.M.K. Ismail, S.L. Rodgers, Carbon 30 (1992) 229.
[31] G. Orlandi, F. Negri, Photochem. Photobiol. Sci. 1 (2002) 289.
[32] O. Berne, A.G.G.M. Tielens, Proc. Nat. Acad. Sci. U.S.A. 109 (2012) 401.
[33] M.C. McCarthy, C.A. Gottlieb, H. Gupta, P. Thaddeus, Astrophys. J. 652 (2006) L141.